

See discussions, stats, and author profiles for this publication at: <https://www.researchgate.net/publication/225677685>

Core-shell nanostructures and nanocomposites of Ag@TiO₂: Effect of capping agent and shell thickness on the optical properties

ARTICLE in JOURNAL OF NANOPARTICLE RESEARCH · MARCH 2009

Impact Factor: 2.18 · DOI: 10.1007/s11051-009-9663-5

CITATIONS

9

READS

151

3 AUTHORS:



Sonalika Vaidya

University of Delhi

21 PUBLICATIONS 427 CITATIONS

SEE PROFILE



Amitava Patra

Indian Association for the Cultivation of Science

172 PUBLICATIONS 4,135 CITATIONS

SEE PROFILE



Ashok K. Ganguli

Indian Institute of Technology Delhi

312 PUBLICATIONS 2,930 CITATIONS

SEE PROFILE

Band Gap Tuning of ZnO/In₂S₃ Core/Shell Nanorod Arrays for Enhanced Visible-Light-Driven Photocatalysis

Sunita Khanchandani,[†] Simanta Kundu,[‡] Amitava Patra,[‡] and Ashok K. Ganguli^{*,†,§}

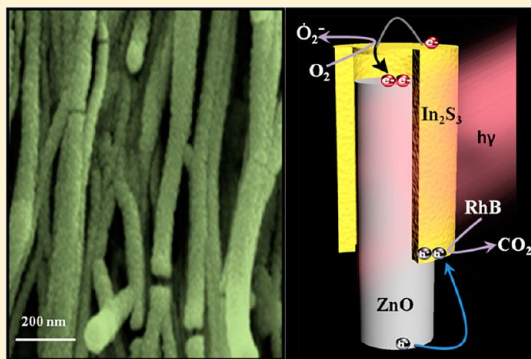
[†]Department of Chemistry, Indian Institute of Technology, Hauz Khas, New Delhi 110016, India

[‡]Department of Materials Science, Indian Association for the Cultivation of Science, Kolkata 700 032, India

[§]Institute of Nano Science & Technology, Phase X, Mohali, Punjab 160062, India

S Supporting Information

ABSTRACT: We report an efficient and environmentally benign one-dimensional ZnO/In₂S₃ core/shell nanostructure to be used as a photocatalyst to overcome the drawback of low photocatalytic efficiency brought by electron–hole recombination and narrow photoresponse range. In₂S₃ nanoparticles were successfully grown on the ZnO nanorods by the surface functionalization method using citric acid as a surface-functionalizing agent. The photocatalytic activity under visible light to degrade rhodamine B (RhB) was enhanced by these core/shell nanostructures due to the formation of heterojunctions, which prolong the separation of photogenerated electrons and holes. The photocatalytic degradation of RhB dye was found to be 83.7, 2.7, and 35.0% for the ZnO/In₂S₃ core/shell nanorod arrays, ZnO nanorods, and In₂S₃ nanoparticles, respectively, under visible light irradiation. Photoconductivity studies showed a 6-fold enhancement in photocurrent (compared to the dark current) for the core/shell nanorod arrays. Moreover, these core/shell nanostructures could be reused for degradation of RhB during a three-cycle experiment without significant decrease in the photocatalytic activity which is very important for these ZnO/In₂S₃ core/shell nanorod arrays to be of practical use in environmental applications.



INTRODUCTION

Efficient, environmentally benign, and low-cost approaches for removal of organic compounds has been one of the current research interests. Finding new approaches of reducing environmental pollution is a great challenge, and as a result, several techniques for the degradation of water contaminants have been developed.¹ Photocatalytic processes represent an attractive strategy for renewable energy generation and environmental remediation. Photocatalytic degradation that uses visible or ultraviolet light as an irradiating source is considered as a key method of water decontamination, as it can bring fast and complete mineralization of pollutants without leaving any harmful residues and has recently become a vital technology. According to the thermodynamic requirement of a photocatalytic reaction, the redox potential of the valence band (VB) hole must be sufficiently positive to generate hydroxyl radicals (OH•) and that of the conduction band (CB) electron must be sufficiently negative to generate superoxide radical anions (O₂^{•-}). ZnO and TiO₂ have been researched intensively as practically applicable materials in photocatalysis, because of their suitable band gap energy and favorable band gap positions compared to other materials.² In particular, nanostructured ZnO exhibits a few distinct advantages over TiO₂, including good carrier mobility, simple tailoring of the structure, and facile and low-cost large-scale manufacturing.³ However, there are two major drawbacks associated with semiconductor

photocatalysts like ZnO and TiO₂. First, the recombination of photogenerated electrons and holes is too fast, which results in low quantum efficiencies and limits the photocatalytic potential of ZnO. Second, the low efficiency for utilizing the visible range of the solar spectrum, which would greatly hinder the commercialization of such a technology.⁴ To increase the photocatalytic reaction rates, the photogenerated electrons and holes must be separated into different locations on the catalyst. This can be achieved by building junctions and chemical potential gradients in the catalyst that tend to separate the electrons and holes into two different regions of the catalyst.⁵ Toward this end, ZnO based nanostructures sensitized with inorganic semiconductor nanocrystals such as CdS,⁶ In₂S₃,⁷ CdSe,⁸ PbS,⁹ InP,¹⁰ Ag₂S,¹¹ and Bi₂S₃¹² can generate multiple electron–hole pairs per photon and consequently enhance the photocatalytic efficiency. For an efficient electron transfer between the sensitizer (here In₂S₃) and photocatalyst (ZnO), the energy level of the conduction band of the photocatalyst must be lower than that of the sensitizers. Thus, the electrons created in sensitizers are subsequently injected into the photocatalyst conduction band to perform a reduction reaction. The charge injection from the sensitizer into a wide-band gap

Received: October 23, 2012

Revised: February 22, 2013

Published: February 25, 2013



semiconductor can lead to efficient and longer charge separation by decreasing the recombination of electron–hole pairs.¹³ Among the most widely used inorganic semiconductor sensitizers, In_2S_3 is an excellent candidate due to its nontoxicity, good stability, narrow band gap (2.0–2.3 eV), and high carrier mobility. In_2S_3 is also used as a buffer layer to replace the environmentally unfriendly CdS buffer layer in $\text{Cu}(\text{In,Ga})\text{Se}_2$ (CIGS) thin film solar cells, where it acts as an n-type semiconductor to form a heterojunction with p-type CIGS. In addition, In_2S_3 forms a typical type-II band alignment with ZnO, allowing effective injection of photogenerated electrons from In_2S_3 into ZnO and increasing the probability of absorption of radiation in the visible range. We have successfully prepared ZnO/ In_2S_3 core/shell photocatalyst by a soft chemical approach, and the results reveal that the combination of narrow band gap with wide band gap semiconductor enhances their photocatalytic abilities. Strothkämper et al.¹⁴ have reported the fabrication of ZnO/ In_2S_3 core/shell nanorod heterojunctions by spray ion layer gas reaction and studied their optical properties. To the best of our knowledge, however, there is no report regarding ZnO/ In_2S_3 core/shell nanorod arrays as an efficient visible-light activated photocatalyst.

In the present work, we demonstrate the surface-functionalized synthesis route of the type-II ZnO/ In_2S_3 core/shell nanorod arrays and have studied the optical, electrical, and photocatalytic properties of ZnO/ In_2S_3 core/shell nanorod arrays. It is found that these core/shell nanorod arrays show enhanced visible light absorption and photocatalytic activity for degrading rhodamine B (RhB) due to efficient charge separation and high transfer efficiency of photogenerated electrons.

EXPERIMENTAL SECTION

Preparation of ZnO Nanorods. Zinc acetate dihydrate was used as the precursor for synthesizing ZnO nanorods.¹⁵ A total of 0.5 g of the precursor was placed in an alumina crucible, covered by an alumina lid, and then placed in a furnace. The crucible was heated to 300 °C and held for a period of 12 h, producing ZnO nanorods in powder form.

Preparation of In_2S_3 Nanoparticles. In_2S_3 nanoparticles were synthesized¹⁶ using indium nitrate and sodium sulphide as precursors. In a typical procedure, 0.01 mol of indium nitrate, $\text{In}(\text{NO}_3)_3 \cdot 5\text{H}_2\text{O}$ and 0.03 mol of $\text{Na}_2\text{S} \cdot 9\text{H}_2\text{O}$ were, separately, dissolved in 50 mL of double distilled water. Next, the indium solution and the sodium sulphide solution were mixed together and loaded in a 100 mL Teflon autoclave. The reaction mixture was heated at 180 °C for 16 h and then air cooled at room temperature. The yellow product was separated by centrifugation and washed with absolute ethanol.

Preparation of ZnO/ In_2S_3 Core/Shell Nanorod Arrays. The surface functionalization route¹⁷ was used to prepare In_2S_3 -coated ZnO nanorods. First, 0.7 mmol of ZnO nanorods was dispersed in 50 mL of deionized water containing 0.19 mmol of citric acid (CA) under constant stirring. The solution was heated at 40 °C for 2 h and cooled to room temperature gradually. The aqueous solution of ZnO became fluffy, indicating that the ZnO nanorod surfaces were functionalized by the citrate ions. In the next step, a 25 mL aqueous solution of 0.7 mmol of $\text{In}(\text{NO}_3)_3 \cdot 5\text{H}_2\text{O}$ was slowly added drop by drop to the ZnO solution under constant magnetic stirring for 2 h. Finally, 1.4 mmol of $\text{Na}_2\text{S} \cdot 9\text{H}_2\text{O}$ was dissolved in 25 mL of deionized water and slowly added dropwise to the system and

stirred for another 1 h at room temperature. This dropwise injection of precursors is very important to slow down the ion-exchange reaction between $[\text{Zn}^{2+}\text{O}^{2-}]$ ions and $[\text{In}^{3+}\text{S}^{2-}]$ ions through the surface of the ZnO core, since the normal In_2S_3 exchange process is so fast that the ZnO core cannot survive. The solution gradually turned light-yellow (yellowish white), indicating the formation of an In_2S_3 layer over the ZnO nanorods. The products were separated by centrifugation and washed repeatedly with water and alcohol and then dried at 60 °C to obtain the powder.

CHARACTERIZATION

Powder X-ray diffraction studies (PXRD) were carried out on a Bruker D8 Advance diffractometer using Ni-filtered Cu $K\alpha$ radiation. Normal scans were recorded with a step size of 0.02° and step time of 1 s. Raw data was subjected to background correction, and the $K\alpha_2$ lines were stripped off. Crystallite sizes (D , in Å) were estimated from the Scherrer equation:

$$D = K\lambda / \beta \cos \theta \quad (1)$$

where λ is the wavelength of Cu $K\alpha$ radiation, β is the corrected half-width of the diffracted peak, θ is the diffraction angle, and K is equal to 0.9.

The lattice strain was calculated using the Williamson and Hall method¹⁸

$$\beta \cos \theta / \lambda = 1/D + \eta \sin \theta / \lambda \quad (2)$$

where β is the full width at half-maximum (fwhm), θ is the diffraction angle, λ is the X-ray wavelength, D is the crystallite size, and η is the effective strain. The strain is calculated from the slope, and the crystallite size (D) is calculated from the intercept of a plot of $\beta \cos \theta / \lambda$ against $\sin \theta / \lambda$.

The morphology of the samples was studied using a field emission scanning electron microscope (FESEM, JEOL, JSM-6700F). The nanostructures were observed using a transmission electron microscope (JEOL 2010). For the TEM observations, the powders were dispersed in ethanol and ultrasonicated for 15 min. A few drops of this solution were taken on a carbon-coated copper grid. Compositional analysis was performed by energy dispersive X-ray analysis (EDAX) attached to a TEM. The distribution in the size of the nanorods and core/shell system were measured from the FESEM and TEM images. Optical absorption spectra were recorded on a UV-2401 PC Shimadzu spectrophotometer in the wavelength range 300–700 nm by dispersing the samples in ethanol. Photoluminescence (PL) spectra were recorded using a Jobin Yvon-Spex Fluorolog spectrophotometer.

I – V and Photoconductivity Measurements. The samples for obtaining the current–voltage (I – V) plots were prepared by the following procedure.¹⁷ A thin copper wire (0.5 mm diameter) was first placed on a degreased glass substrate. A thin layer (100 nm) of Au was then deposited by sputter coating (using an Eiko IB-2 ion coater), and the copper wire was removed. A two-probe configuration of the electrodes was created on the Au sputtered glass substrate. The powder sample was mixed with alcohol to obtain a smooth paste, which was then coated on the two electrodes and allowed to dry in air to form a thin film with a typical thickness and length of about 0.1 and 5 mm, respectively. The device was put into a chamber, and an electrometer (Keithley 6517B) was connected between the two gold electrodes. The I – V measurement was performed with the electrometer at room temperature. Photocurrent measurement was performed with a 150 W Newport-Stratford

Solar Simulator model 76500 using white light under 1 sun (AM 1.5 G) illumination at 100 mW cm^{-2} .

Photocatalytic Experiments. The photocatalytic properties of ZnO nanorods, In_2S_3 nanoparticles, and ZnO/ In_2S_3 core/shell nanorod arrays were measured by the degradation of rhodamine B (RhB) in aqueous solution under visible light irradiation. In a typical process, 20 mg of the sample was dispersed in 80 mL of $1.0 \times 10^{-5} \text{ M}$ RhB aqueous solution. The dye solution with the catalyst was stirred in the dark for 2 h until the equilibrium adsorption was attained. No significant decrease in the concentration of the dye was observed after 2 h for all the experiments. A 500 W Xe lamp with a 420 nm cutoff filter was used as the visible light source. Experiments without visible light irradiation in the presence of the catalyst, and experiments with visible light irradiation in the absence of catalyst, showed no degradation of dye. The solution was then exposed to visible light irradiation with a perfectly transparent glass plate to cover the top. The beaker was kept in an ice-cold water bath to ensure that the temperature was maintained and the degradation was the result of photocatalytic activity only. Samples were taken at intervals of 20 min and centrifuged to remove the catalyst particles. The clear supernatant solution was analyzed in a UV–vis spectrophotometer (measured at 555 nm) to determine the concentration of RhB.¹⁹ The degradation efficiency of the photocatalyst can be defined as follows:

$$\text{Degradation (\%)} = (1 - C/C_0) \times 100\% \quad (3)$$

where C_0 is the concentration of RhB at adsorption equilibrium and C is the residual concentration of RhB at different illumination intervals.

The photodegradation of RhB follows pseudo-first-order kinetics, which can be expressed as

$$\ln(C_0/C) = kt \quad (4)$$

where k (min^{-1}) is the degradation rate constant.

Each data point and error bar represents the mean and the standard errors, respectively, of independent triplicates, and the error propagation was calculated wherever necessary.

Analysis of Hydroxyl Radicals ($\text{OH}\bullet$). Hydroxyl radicals ($\text{OH}\bullet$) produced by the photocatalysts under visible light irradiation were measured by the fluorescence method using terephthalic acid (TA) as a probe molecule. A 5 mg portion of ZnO/ In_2S_3 sample was dispersed in 30 mL of a $5 \times 10^{-4} \text{ M}$ TA aqueous solution in a diluted NaOH aqueous solution ($2 \times 10^{-3} \text{ M}$). The resulting suspension was then exposed to visible light irradiation. At regular intervals, 1.2 mL of the suspension was collected and centrifuged to measure the maximum fluorescence emission intensity with an excitation wavelength of 315 nm. This method relies on the fluorescence signal at 425 nm of the hydroxylation of terephthalic acid with $\text{OH}\bullet$ generated at the ZnO/ In_2S_3 interface.²⁰

RESULTS AND DISCUSSION

Figure 1 shows the XRD patterns of the ZnO nanorods and ZnO/ In_2S_3 core/shell nanostructures. The XRD pattern of the uncoated ZnO nanorods shows a highly crystalline hexagonal phase (wurtzite structure) of ZnO (JCPDS card no. 36-1451). In the XRD pattern of core/shell ZnO/ In_2S_3 , additional peaks at 33.60° (102) and 47.41° (110) clearly indicate the existence of the hexagonal phase of the In_2S_3 shell (JCPDS card no. 330623) along with the hexagonal phase of ZnO. A careful analysis of the XRD patterns of the ZnO/ In_2S_3 core/shell

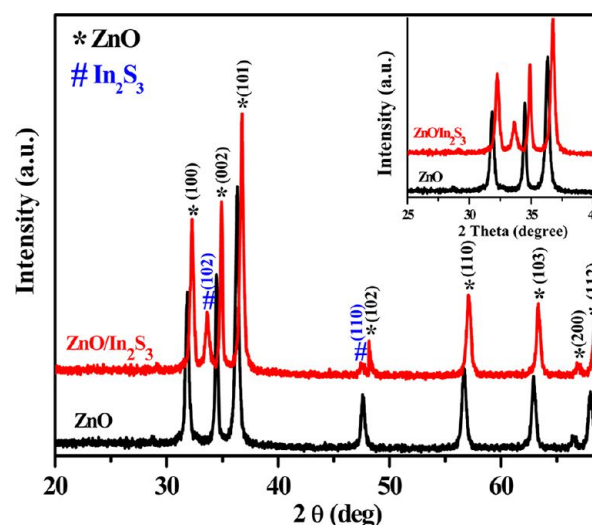


Figure 1. XRD patterns of uncoated ZnO nanorods and ZnO/ In_2S_3 core/shell nanorod arrays. The inset shows the shift in the peak position of the XRD patterns of ZnO/ In_2S_3 compared to pure ZnO.

nanostructures unravels the effect of shell formation on the lattice parameters and the lattice strain of ZnO. The XRD pattern of ZnO nanorods consists of the characteristic hexagonal phase. A gradual shift of the diffraction maxima of ZnO toward larger angles with shell growth is observed. This shift to higher angles in the core/shell structure (inset of Figure 1) is due to a smaller lattice constant of ZnO for ZnO/ In_2S_3 core/shell nanorod arrays compared with bare ZnO nanorods (Table 1). Wang et al.²¹ observed the shift of the diffraction peaks to larger angles located between the cubic CdSe and CdS phase in CdSe/CdS core/shell nanocrystals. Similar changes in the diffraction pattern were also reported for other core/shell nanostructures.^{22–24} Figure 2a shows a plot of $\beta \cos \theta/\lambda$ against $\sin \theta/\lambda$ for pure ZnO nanorods (using eq 2), and the slope is $+0.0033$. The positive slope indicates the tensile strain. The obtained crystallite size is 33.3 nm (from the intercept), which is in good agreement with the calculated value from the Scherrer equation (Table 1). Tensile strain is defined as the deformation along a line segment that increases in length when a load is applied along that line. Figure 2b represents a plot for ZnO/ In_2S_3 core/shell nanorod arrays having a shell thickness of 15 nm, and a negative slope (-0.0020) is obtained. It indicates the presence of compressive strain (-0.2%). The crystallite size is found to be 28.5 nm, which matches well with the calculated value of 27.6 nm using the Scherrer equation. As the shell is grown, the diffraction peaks shift toward smaller d -spacings (larger 2θ).²⁵ This indicates the growth of the In_2S_3 shell which compresses the lattice planes of the ZnO core. Compressive strain is defined as the deformation along a line segment that decreases in length when a load is applied. Results reveal that the surface coating plays an important role in tuning the lattice strain of core/shell nanostructures. A similar kind of observation was observed for the Eu^{3+} -coated TiO_2 particles.²⁶

The morphology of the as-prepared ZnO and ZnO/ In_2S_3 sample was investigated in detail by FESEM and TEM images. Figure 3a shows the FESEM image of the uncoated ZnO nanorods with an average diameter of about $100 \pm 5 \text{ nm}$ and with smooth surfaces. After the growth of the In_2S_3 shell, the surface of the ZnO nanorods was no longer smooth. Instead, the nanorods were decorated with numerous secondary nanoparticles of In_2S_3 , as shown in Figure 3b. The TEM

Table 1. Crystallite Size, Cell Parameters, and Lattice Strain of ZnO and ZnO/In₂S₃ Core/Shell Nanorod Arrays

sample	shell thickness (nm)	crystallite size (Scherrer equation) (nm)	crystallite size (Williamson and Hall method) (nm)	cell parameter (Å)	lattice strain (%)
ZnO		32.5	33.3	$a = 3.254(2)$, $c = 5.216(4)$	+0.337
ZnO/In ₂ S ₃	15 (± 2)	27.6	28.5	$a = 3.250(2)$, $c = 5.212(2)$	−0.200

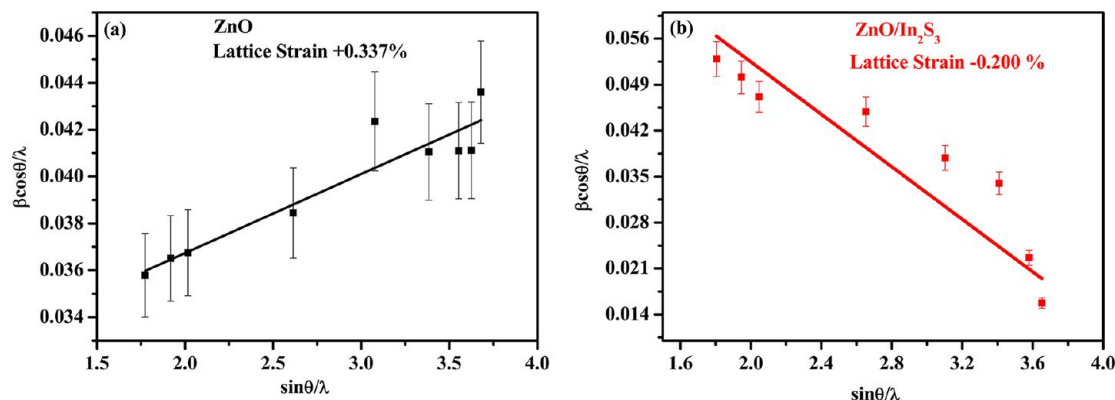
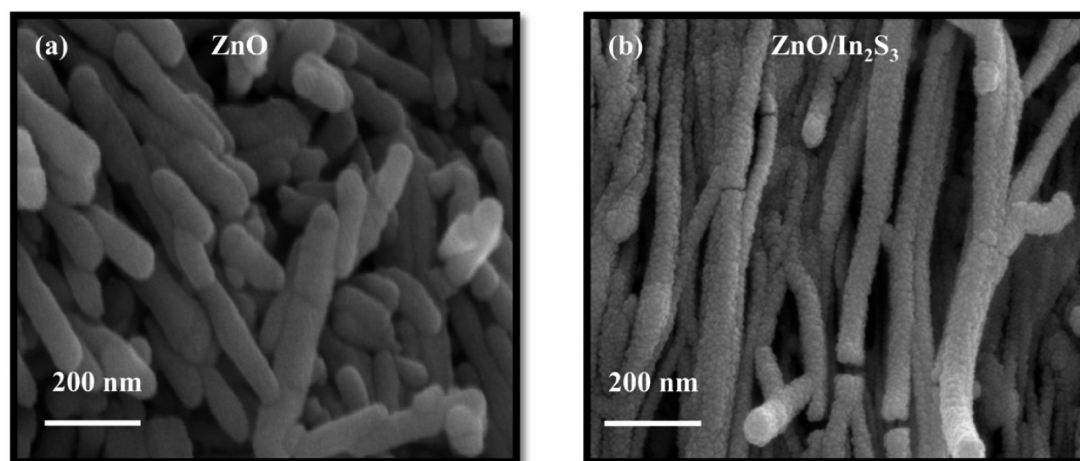
Figure 2. Williamson–Hall plot for (a) pure ZnO and (b) ZnO/In₂S₃ core/shell nanorod arrays.Figure 3. FESEM images of (a) ZnO nanorods and (b) ZnO/In₂S₃ core/shell nanorod arrays.

image (Figure 4a) of uncoated ZnO nanorods shows an average diameter of 100 ± 6 nm and a length of 500–600 nm with smooth surfaces. The apparent contrast in the TEM micrograph between the ZnO core and the In₂S₃ shell offers evidence for the formation of ZnO/In₂S₃ core/shell nanorod arrays, as shown in Figure 4b. The thickness of the shell layer was calculated to be 15 ± 2 nm. Shell growth of In₂S₃ on ZnO is further confirmed by the HRTEM images (Figure 4c). The high-resolution bright field TEM image (Figure 4c) clearly shows the sharp interface between the nanorod core and the shell. The periodicity of the fringes obtained from the HRTEM studies of the core is 0.247 nm, corresponding to the (101) planes of hexagonal ZnO. The nanoparticles of the In₂S₃ shell show a fringe spacing of 0.269 nm that corresponds to the reported value for the (102) plane of hexagonal In₂S₃. The energy dispersive X-ray spectroscopy (EDX) of ZnO/In₂S₃ core/shell nanorod arrays revealed that most of the Zn and O atoms were found in the core region, and In and S atoms were found in the shell region, as shown in the Supporting

Information (Figure S1a and b), respectively, which is as expected.

The optical absorption spectra of the uncoated ZnO nanorods, In₂S₃ nanoparticles, and core/shell nanorod arrays are shown in Figure 5a. The uncoated ZnO shows an absorption at 373 nm (3.32 eV).¹⁵ Compared with bare ZnO nanorods, the light absorption ability of the ZnO/In₂S₃ core/shell nanorod arrays is significantly enhanced due to the shift of the absorption spectrum to the visible-light region (maxima at 445 nm) owing to the incorporation of In₂S₃. Thus, the ZnO/In₂S₃ core/shell nanorod arrays are promising as photocatalysts under visible light compared to pure ZnO which has an insignificant absorption response to visible light due to its wide band gap.

Figure 5b shows the PL spectra of the ZnO nanorods and ZnO/In₂S₃ core/shell nanorod arrays recorded using an excitation at 325 nm. In₂S₃ nanoparticles were excited at 400 nm. In our studies (Figure 5b, PL of ZnO), the strong UV emission at 381 nm originated from the excitonic recombination corresponding to the band edge emission of ZnO. A broad

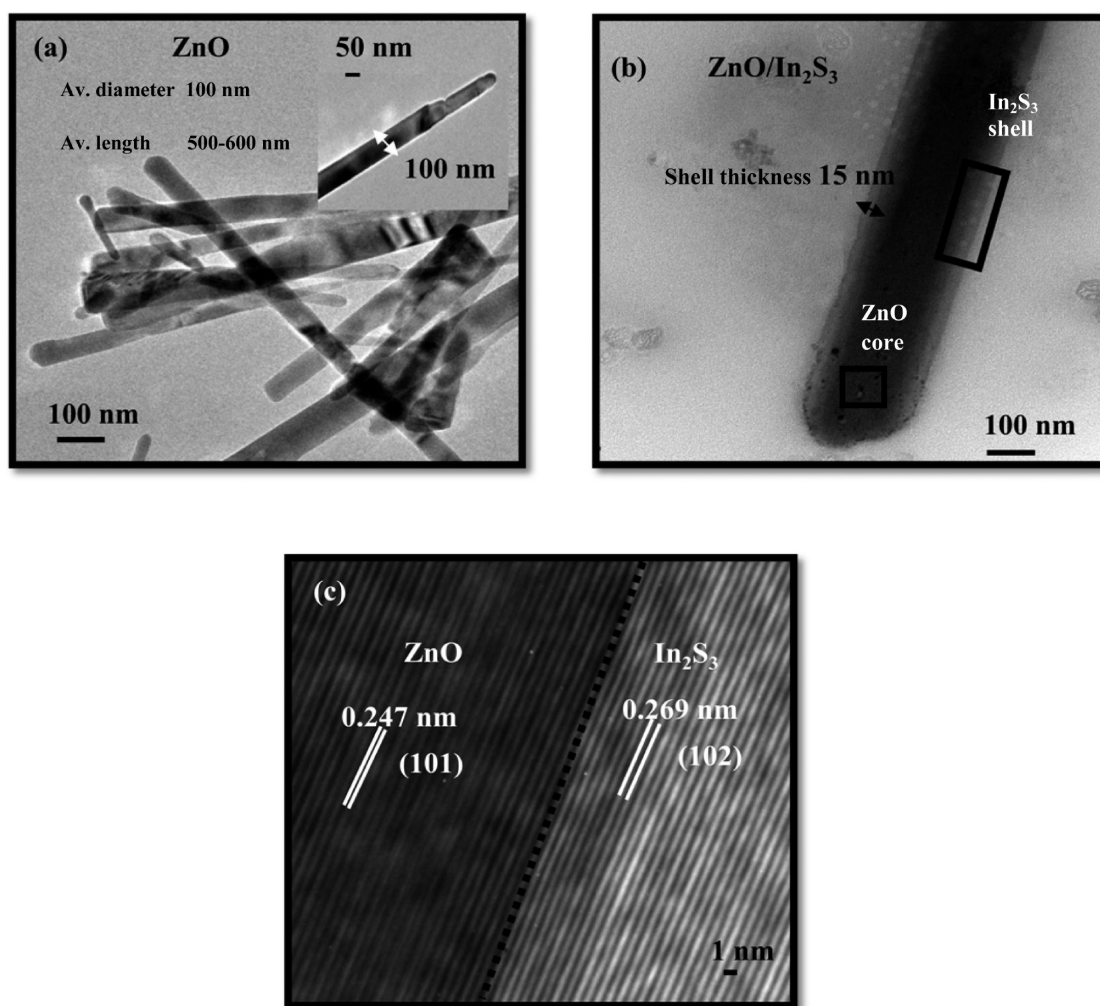


Figure 4. TEM images of (a) ZnO nanorods, (b) ZnO/In₂S₃ core/shell nanorod arrays, and (c) HR-TEM image of ZnO/In₂S₃ core/shell nanorod arrays showing lattice planes.

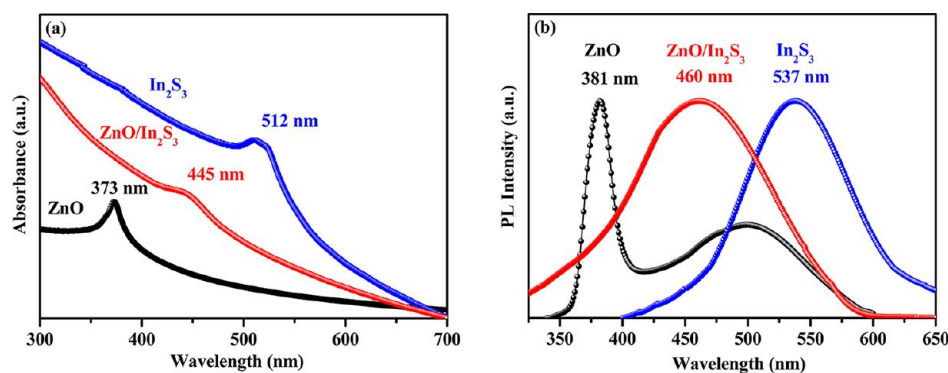


Figure 5. (a) Optical absorption spectra and (b) photoluminescence spectra of uncoated ZnO nanorods, In₂S₃ nanoparticles, and ZnO/In₂S₃ core/shell nanorod arrays.

peak is observed at a lower energy of 490–520 nm.¹⁵ This peak probably results from one of the following:¹⁵ (1) transition from CB to deep acceptor levels (O_i or O_{Zn}); (2) transition from deep donor levels (V_OZn_i) to VB; (3) transition from shallow donor levels (Zn_i) to shallow acceptor levels (V_{Zn} and O_i), where V_{Zn} = vacant Zn, V_O = vacant O, Zn_i = interstitial Zn, O_i = interstitial O, V_OZn_i = complex of V_O and Zn_i , O_{Zn} = substitution of O at Zn sites.

Pure hexagonal In₂S₃ nanoparticles exhibit an emission peak around 537 nm (2.31 eV).²⁷ The growth of the In₂S₃ shell on the ZnO core causes almost immediate quenching of the emission of ZnO, and a new emission peak around 460 nm appears. The significant red shift in the absorption and emission spectra from core/shell samples also confirms that a relevant percentage of the shell is composed of In₂S₃. Given the small energy difference between the conduction band offset between In₂S₃ and ZnO (0.20 eV in the bulk limit), the photogenerated

electrons in ZnO/In₂S₃ core/shell nanorod arrays can easily tunnel from the In₂S₃ shell into the ZnO core; thus, the core/shell heterostructure can reduce the electron–hole recombination probability and enhance the visible-light absorption ability. It should be noted that when the In₂S₃ precursors (Indium nitrate and sodium sulphide) were not added in a dropwise manner to the solution containing the ZnO NRs, the growth of pure In₂S₃ nanoparticles increased instead of In₂S₃ shell formation. The PL band of resulting core/shell structures shifted to 537 nm, corresponding to the spectral signature of pure In₂S₃, indicating the completion of the ion-exchange reaction between [Zn²⁺O²⁻] ions and [In³⁺S²⁻] ions under this fast growth condition, and the consumption of the core results in pure In₂S₃ NRs.²⁸

Figure 6 shows the dark and photocurrent of ZnO/In₂S₃ core/shell nanorod arrays in normal conditions where the

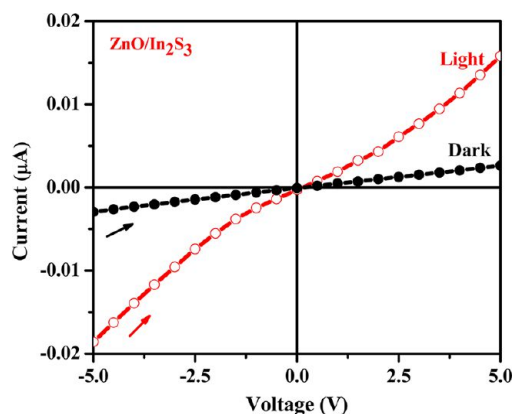


Figure 6. Dark and photocurrent measurement plots of ZnO/In₂S₃ core/shell nanorod arrays in forward bias.

voltage is applied between Au and Au terminals in the forward direction.²⁹ The photocurrent of ZnO/In₂S₃ core/shell nanorod arrays shows 6-fold enhancement compared to the dark current. A type-II interaction between the conduction band edges of the In₂S₃ and the conduction band of ZnO provides an efficient charge separation in the ZnO/In₂S₃ heterostructure. In the presence of light; these charge carriers are generated and efficiently transferred to the electrodes when voltage is applied. This charge separation in the ZnO/In₂S₃ heterostructure enhances the mobility of the charge carriers.³⁰ This charge separation phenomenon is the reason for the enhanced photocatalytic activity of the ZnO/In₂S₃ heterostructure compared to the ZnO nanorods, or the In₂S₃ nanoparticles which are discussed later.

The photocatalytic activity of the ZnO/In₂S₃ core/shell nanorod arrays on the degradation of RhB (Figure 7a) was compared with that of bare ZnO nanorods and In₂S₃ nanoparticles under visible-light irradiation (Figure 7b). The ZnO/In₂S₃ core/shell nanorod arrays exhibited significantly enhanced photocatalytic activity as compared with both bare ZnO and In₂S₃. Bare ZnO has negligible photocatalytic activity under visible-light irradiation due to its wide band gap, whereas the introduction of In₂S₃ into ZnO enhances the photocatalytic activity of the core/shell nanostructures. The photodegradation efficiency of RhB reached 83.7 (±4.0)% in the presence of the core/shell nanorod arrays after 100 min of visible light irradiation, whereas it was only 35 (±1.7)% for the In₂S₃ nanoparticles (Figure 7c) within the same period, indicating

that the ZnO/In₂S₃ core/shell nanorod arrays are much superior as a catalyst. The kinetics of degradation of RhB under visible light irradiation was also investigated. Figure 7d shows a linear relationship between $\ln(C_0/C)$ and reaction time, indicating that the photodegradation of RhB follows first-order kinetics. The apparent rate constants were determined as 3.09×10^{-4} ($\pm 0.2 \times 10^{-4}$), 4.20×10^{-3} ($\pm 0.15 \times 10^{-3}$), and 1.74×10^{-2} ($\pm 0.15 \times 10^{-2}$) min⁻¹ for ZnO, In₂S₃, and ZnO/In₂S₃, respectively. The order of rate constant is as follows: ZnO/In₂S₃ > In₂S₃ > ZnO. The photocatalytic activity of the ZnO/In₂S₃ core/shell nanorod arrays is about 5 times higher than In₂S₃ nanoparticles and 56 times higher than ZnO nanorods. The results of optical, electrical, and photocatalytic properties of ZnO, In₂S₃, and ZnO/In₂S₃ core/shell nanorod arrays are summarized in Table 2.

Photocatalytic Mechanism. It has been widely accepted that hydroxyl radicals (OH•) generated by the illumination of photocatalyst are the main species responsible for the degradation of pollutant molecules. According to the thermodynamic requirement for generation of OH•, the VB and CB of the semiconductor photocatalyst should be positioned in such a way that the oxidation potential of the hydroxyl radical ($E^\circ \text{H}_2\text{O}/\text{OH}^\bullet = 2.8 \text{ V}$ vs normal hydrogen electrode (NHE)) and the reduction potential of superoxide radicals ($E^\circ \text{O}_2/\text{O}_2^{\bullet-} = -0.28 \text{ V}$ vs NHE) lie well within the band gap of the photocatalyst.² As we know, ZnO has no absorption response to visible light due to its wide band gap; thus, the light absorption of ZnO/In₂S₃ core/shell heterostructures was solely contributed by the In₂S₃ component in the photocatalysis experiments. To approach the mechanism of the enhanced activity of ZnO/In₂S₃ core/shell nanorod arrays, the relative band positions of the two semiconductors were investigated, since the band–edge potential plays a crucial role in determining the transfer of photoexcited charge carriers in a heterojunction. The conduction band (CB) (lower bound) (E_{CB}) was calculated empirically according to the formula³¹

$$E_{\text{CB}} = X - 0.5E_{\text{g}} + E_0 \quad (5)$$

where E_{g} is the band gap energy of the semiconductor, E_0 is the scale factor relating the reference electrode redox level to the absolute vacuum scale ($E_0 = -4.5 \text{ eV}$ for normal hydrogen electrode), and X is the electronegativity of the semiconductor, which can be expressed as the geometric mean of the absolute electronegativity of the constituent atoms. The X values for ZnO and In₂S₃ are 1.885 and 1.400 eV, respectively, and the band gap energies of ZnO and In₂S₃ are 3.37 and 2.00 eV, respectively. Given the equation above, the conduction band bottom (E_{CB}) of ZnO and In₂S₃ is calculated to be -4.30 and -4.10 eV, respectively. Correspondingly, the tops of the valence bands (E_{VB}) of ZnO and In₂S₃ are -7.67 and -6.10 eV, respectively. Thus, the conduction band bottom (E_{CB}) of In₂S₃ is higher than that of ZnO and the valence band top (E_{VB}) of In₂S₃ is higher than that of ZnO. The conduction band (CB) bottom and the valence band (VB) top of ZnO lie at -0.2 and 3.17 V with respect to NHE, and the values for In₂S₃ are -0.4 and 1.6 V. Thus, individually, ZnO and In₂S₃ do not fulfill the thermodynamic requirement for the OH• generation. Considering the band gap of In₂S₃ ($E_{\text{g}} = 2.00 \text{ eV}$) is lower than that of ZnO ($E_{\text{g}} = 3.37 \text{ eV}$) but the conduction band (CB) and the valence band (VB) of In₂S₃ are higher than those of ZnO, an efficient heterostructure could be formed for the separation of photogenerated charge carriers when coupled together. The calculated results indicate that the band disposition of the

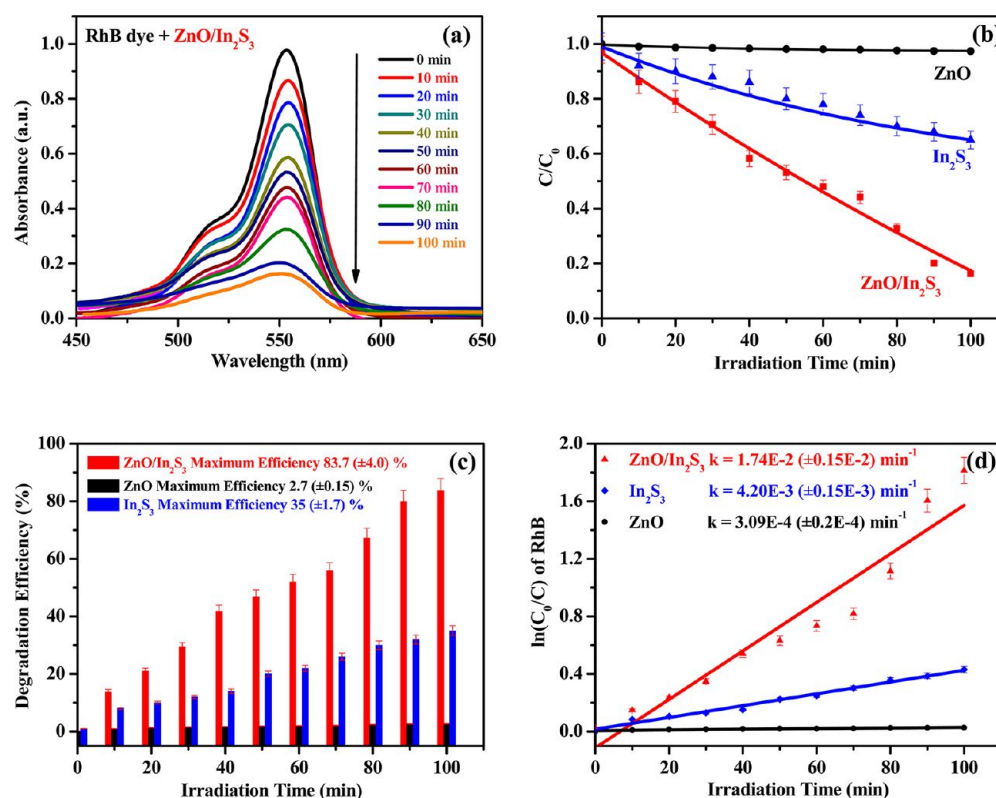


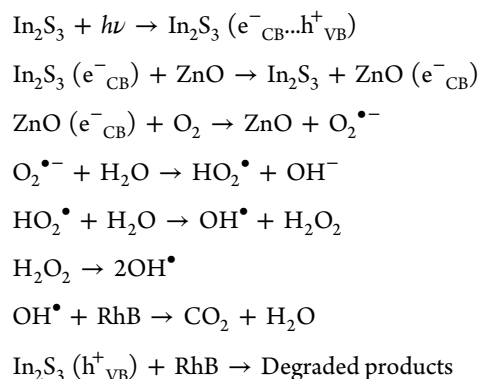
Figure 7. (a) Absorption spectrum of a solution of RhB in the presence of ZnO/In₂S₃ core/shell nanorod arrays under exposure to visible light, (b) photocatalytic performances of ZnO nanorods, In₂S₃ nanoparticles, and ZnO/In₂S₃ core/shell nanorod arrays for the degradation of RhB solution under visible light, (c) degradation efficiency of ZnO nanorods, In₂S₃ nanoparticles, and ZnO/In₂S₃ core/shell nanorod arrays on the photodegradation of RhB as a function of time, and (d) plot of $\ln(C_0/C)$ as a function of visible irradiation time for photocatalysis of RhB solution containing ZnO nanorods, In₂S₃ nanoparticles, and ZnO/In₂S₃ core/shell nanorod arrays.

Table 2. Optical and Photocatalytic Properties of ZnO, In₂S₃ and ZnO/In₂S₃ Core/Shell Nanorod Arrays

sample	shell thickness (nm)	absorption band (nm)	PL band (nm)	photocatalytic efficiency (%)	rate constant (min ⁻¹)
ZnO	-	373	381	2.70 (±0.15)	3.09E ⁻⁴ (±0.2E ⁻⁴)
In ₂ S ₃	-	512	537	35.0 (±1.7)	4.20E ⁻³ (±0.15E ⁻³)
ZnO/In ₂ S ₃	15 (±2)	445	460	83.70 (±4.0)	1.74E ⁻² (±0.15E ⁻²)

ZnO/In₂S₃ core/shell nanorod arrays is advantageous for the separation and transportation of charge carriers. Consequently, the efficient charge separation increased the lifetime of the charge carriers and hence enhanced the efficiency of the charge transferred to the adsorbed substrates, leading to higher photocatalytic activity of the ZnO/In₂S₃ core/shell nanorods. Although ZnO/In₂S₃ core/shell nanorods contain much less of the visible light absorbing In₂S₃ component, its enhanced photocatalytic performance as compared with the bare In₂S₃ nanoparticles is correlated to the type-II band alignment of the core/shell nanostructures. This is shown schematically in Figure 8 where the type-II configuration of the core/shell heterostructure reduces the electron–hole recombination probability, enables one to increase the electron mobility, and efficiently separates the photogenerated electrons and holes at the ZnO/In₂S₃ interface. Under visible light irradiation, photogenerated electrons in In₂S₃ moved freely to the ZnO (core), while the photogenerated holes are left in the valence band of In₂S₃ (shell). It is important to mention here that the band alignments are an estimate and are not based on any direct measurement, and in particular, charge transfer effects at the interface³² have been neglected. Dissolved oxygen molecules react with the surface of the ZnO electrons (e⁻) to

yield superoxide radical anions (O₂^{•-}), which on protonation generate the hydroperoxy radicals (HO₂[•]). This produces hydroxyl radical (OH[•]) in water which is a strong oxidizing agent to decompose effectively the organic pollutants such as RhB. The mechanism for the photocatalytic degradation of RhB can be proposed as follows:



where e⁻_{CB} and h⁺_{VB} stand for the electron in the conduction band and hole in the valence band, respectively.

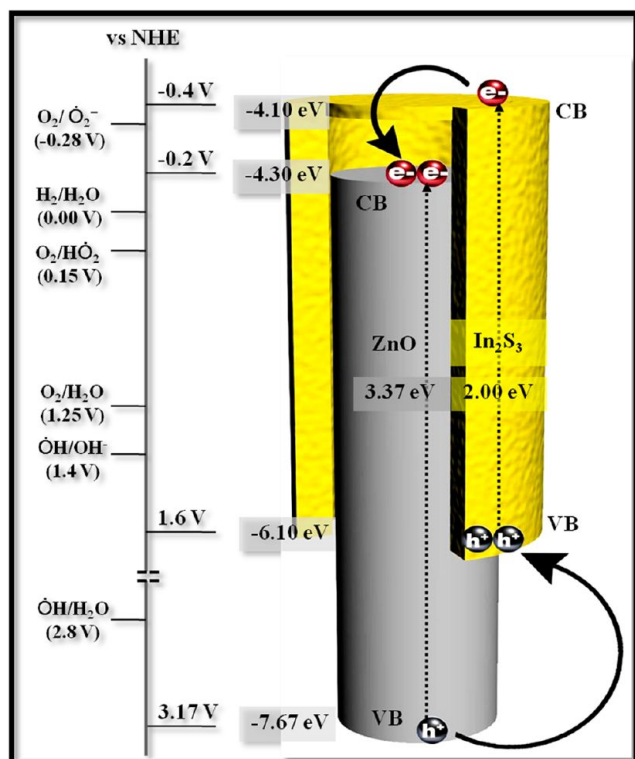


Figure 8. Schematic illustration of band gap energy and band gap positions for the ZnO/In₂S₃ core/shell nanorod arrays showing the type-II band gap alignment and electron–hole pair generation by incident photons along with the redox potential for OH• generation.

To establish the mechanism of the photocatalysis, the formation of OH• on the surface of photocatalysts was detected by the fluorescence technique using terephthalic acid (TA) as a probe molecule, which readily reacts with OH• to produce the highly fluorescent product, 2-hydroxyterephthalic acid (TAOH). The fluorescence intensity of TAOH is proportional to the amount of OH• produced on the surface of photocatalysts. The maximum emission intensity in fluorescence spectra was recorded at 425 nm by the excitation at 315 nm. Using TA as the probe molecule, the OH• produced by ZnO/In₂S₃ core/shell nanostructures under visible light irradiation was measured by the fluorescence method and the results are shown in Figure 9a. It can be seen that the fluorescence intensity increases gradually with increasing

irradiation time, indicating OH• is formed during this photocatalytic process under visible light irradiation. Figure 9b shows an almost linear increase in fluorescence intensity against illumination time at 425 nm. Consequently, we can conclude that OH• radicals formed at the ZnO/In₂S₃ interface are proportional to the light illumination time obeying zero-order reaction rate kinetics.³³ The formation rate of the OH• radicals could be expressed by the slope of the plot shown in Figure 9b. However, no fluorescence increase is observed in the absence of visible light or ZnO nanorods. This suggests that the fluorescence signal is only caused by the reaction of terephthalic acid with OH• formed on the interface of the ZnO/In₂S₃ core/shell nanorod arrays during visible-light irradiation. Generally, the greater the formation rate of OH• radicals, the greater is the separation efficiency of electron–hole pairs. Hence, the photocatalytic activity has a positive correlation with the formation rate of OH• radicals.²⁰

To test the stability and reusability of ZnO/In₂S₃ core/shell nanorod arrays as a photocatalyst, cycling experiments in the photodegradation of RhB under visible light irradiation were monitored. As illustrated in Figure 10a, after another three cycles of photodegradation of RhB, the photocatalytic behavior of ZnO/In₂S₃ heterostructures exhibited minor loss of activity. The degradation efficiency of core/shell nanostructures on photodegradation of RhB after the first, second, and third cycles was found to be 74 (±3.7), 68 (±3.4), and 62 (±3.1)%, respectively (Figure S2, Supporting Information). The efficiency of the catalyst is observed to be lowered by the third cycle which could be due to photobleaching of the surface.^{34,35} The XRD pattern of ZnO/In₂S₃ after three photocatalytic reactions (Figure 10b) reveals that the phase and structure remain intact. We have also investigated the morphology of the samples after the three photocatalytic cycles. The FESEM (Figure S3a, Supporting Information) and TEM (Figure S3b, Supporting Information) images of ZnO/In₂S₃ photocatalyst after three cycles reveal that there is no significant change in the morphology of the photocatalyst. These results indicate that the ZnO/In₂S₃ heterostructure photocatalyst is sufficiently stable and not deactivated during the photodegradation of the organic dye. It is confirmed by our experiments that the core/shell nanorod arrays of ZnO/In₂S₃ having a shell thickness of 15 nm display enhanced photocatalytic activity for degradation of RhB by visible light irradiation, which is due to the highly uniform and complete coverage of ZnO nanorods by In₂S₃ nanoparticles. Thus, ZnO

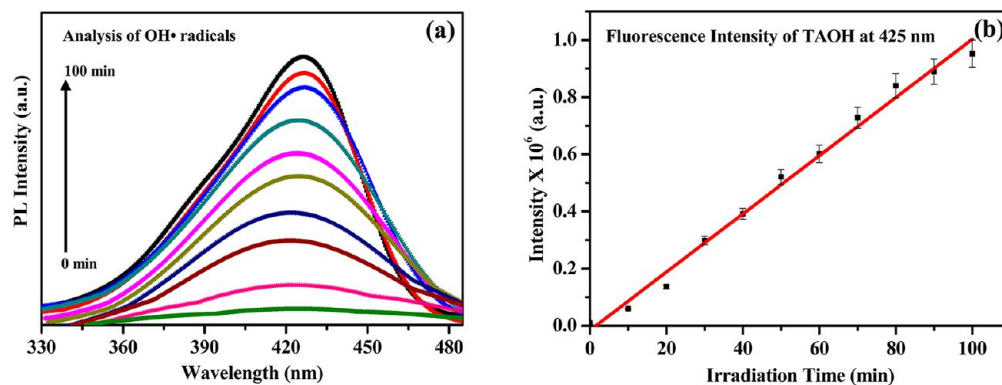


Figure 9. (a) Fluorescence spectral changes measured during illumination of ZnO/In₂S₃ core/shell nanorod arrays in a basic solution of terephthalic acid (excitation at 315 nm) and (b) fluorescence intensity at 425 nm against illumination time for TAOH (2-hydroxyterephthalic acid).

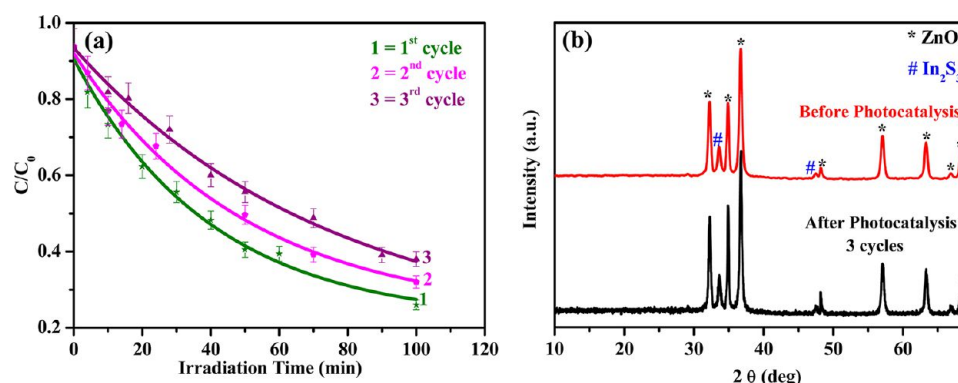


Figure 10. (a) Recyclability of the photocatalytic decomposition of RhB for ZnO/In₂S₃ core/shell nanorod arrays under visible light and (b) XRD patterns of ZnO/In₂S₃ core/shell nanorod arrays before and after photocatalytic reaction.

nanorods sensitized by In₂S₃ shell can be used to fabricate efficient photocatalysts for the degradation of organic pollutants under sunlight and can also be used as solar-energy-conversion materials.

CONCLUSIONS

ZnO/In₂S₃ type-II core/shell nanorod arrays were prepared by a surface-functionalized method. The core/shell photocatalyst exhibits significantly enhanced photocatalytic activity in degradation of RhB under visible light irradiation, which is 5 times higher than In₂S₃ nanoparticles and 56 times higher than ZnO nanorods. The enhanced activity is attributed to the effective separation of electron–hole pairs due to the formation of heterojunctions between the two semiconductors. Such a core/shell photocatalyst is promising for water remediation. Significantly, the enhanced performance demonstrates the importance of evaluating new photocatalysts (core/shell nanostructures). This work provides a new path to fabricate heterostructured materials for photocatalytic and photovoltaic applications.

ASSOCIATED CONTENT

Supporting Information

Figure S1 shows EDX analysis of the marked region in Figure 4b corresponding to (a) core and (b) shell of ZnO/In₂S₃ nanostructures. Figure S2 shows the percent degradation efficiency of ZnO/In₂S₃ core/shell nanorod arrays with increasing number of catalytic cycle. Figure S3 shows (a) FESEM and (b) TEM images of ZnO/In₂S₃ after three photocatalytic cycles. This material is available free of charge via the Internet at <http://pubs.acs.org>.

AUTHOR INFORMATION

Corresponding Author

*E-mail: ashok@chemistry.iitd.ernet.in. Phone: 91-11-26591511. Fax: 91-11-26854715.

Notes

The authors declare no competing financial interest.

ACKNOWLEDGMENTS

A.K.G. and A.P. thank Department of Science & Technology, Council of Scientific and Industrial Research, and DIT, Govt. of India for financial support. A.K.G. also thanks DRDO for financial support. S. Khanchandani and S. Kundu thank Council of Scientific and Industrial Research, Govt. of India for a

fellowship. We thank Prof. A. J. Pal and Mr. S. K. Saha for the photoconductivity measurement.

REFERENCES

- (1) Wu, T.; Zhou, X.; Zhang, H.; Zhong, X. Bi₂S₃ Nanostructures: A New Photocatalyst. *Nano Res.* **2010**, *3*, 379–386.
- (2) Vinu, R.; Madras, G. J. Environmental Remediation by Photocatalysis. *J. Indian Inst. Sci.* **2010**, *90*, 189–230.
- (3) Shen, Q.; Zhao, X.; Zhou, S.; Hou, W.; Zhu, J.-J. ZnO/CdS Hierarchical Nanospheres for Photoelectrochemical Sensing of Cu²⁺. *J. Phys. Chem. C* **2011**, *115*, 17958–17964.
- (4) Wang, J.; Jing, L. Q.; Xue, L. P.; Qu, Y. C.; Fu, H. G. Enhanced Activity of Bismuth-Compounded TiO₂ Nanoparticles for Photocatalytically Degrading Rhodamine B Solution. *J. Hazard. Mater.* **2008**, *160*, 208–212.
- (5) Liu, B.; Khare, A.; Aydil, E. S. TiO₂-B/Anatase Core-Shell Heterojunction Nanowires for Photocatalysis. *Appl. Mater. Interfaces* **2011**, *3*, 4444–4450.
- (6) (a) Gerischer, H.; Luebke, M. A Particle Size Effect in the Sensitization of TiO₂ Electrodes by a CdS Deposit. *J. Electroanal. Chem.* **1986**, *204*, 225–227. (b) Khanchandani, S.; Kundu, S.; Patra, A.; Ganguli, A. K. Shell Thickness Dependent Photocatalytic Properties of ZnO/CdS Core–Shell Nanorods. *J. Phys. Chem. C* **2012**, *116*, 23653–23662.
- (7) Gan, X.; Li, X.; Gao, X.; Qiu, J.; Zhuge, F. TiO₂ Nanorod Arrays Functionalized with In₂S₃ Shell Layer by a Low-Cost Route for Solar Energy Conversion. *Nanotechnology* **2011**, *22*, 305601–305607.
- (8) Robel, I.; Subramanian, V.; Kuno, M.; Kamat, P. V. Quantum Dot Solar Cells. Harvesting Light Energy with CdSe Nanocrystals Molecularly Linked to Mesoscopic TiO₂ Films. *J. Am. Chem. Soc.* **2006**, *128*, 2385–2393.
- (9) Plass, R.; Serge, P.; Krüger, J.; Grätzel, M. Quantum Dot Sensitization of Organic-Inorganic Hybrid Solar Cells. *J. Phys. Chem. B* **2002**, *106*, 7578–7580.
- (10) Blackburn, J. L.; Selmarten, D. C.; Ellingson, R. J.; Jones, M.; Micic, O.; Nozik, A. J. Electron and Hole Transfer from Indium Phosphide Quantum Dots. *J. Phys. Chem. B* **2005**, *109*, 2625–2631.
- (11) Xie, Y.; Heo, S. H.; Kim, Y. N.; Yoo, S. H.; Cho, S. O. Synthesis and Visible–Light–Induced Catalytic Activity of Ag₂S-Coupled TiO₂ Nanoparticles and Nanowires. *Nanotechnology* **2010**, *21*, 015703–015710.
- (12) Vogel, R.; Hoyer, P.; Weller, H. Quantum-Sized PbS, CdS, Ag₂S, Sb₂S₃, and Bi₂S₃ Particles as Sensitizers for Various Nanoporous Wide-Bandgap Semiconductors. *J. Phys. Chem.* **1994**, *98*, 3183–3188.
- (13) Zhou, H.; Qu, Y.; Zeida, T.; Duan, X. Towards Highly Efficient Photocatalysts Using Semiconductor Nanoarchitectures. *Energy Environ. Sci.* **2012**, *5*, 6732–6743.
- (14) Strothkämper, C.; Schwarzburg, K.; Schütz, R.; Eichberger, R.; Bartelt, A. Multiple-Trapping Governed Electron Transport and Charge Separation in ZnO/In₂S₃ Core/Shell Nanorod Heterojunctions. *J. Phys. Chem. C* **2012**, *116*, 1165–1173.

- (15) Lin, C.-C.; Li, Y.-Y. Synthesis of ZnO Nanowires by Thermal Decomposition of Zinc Acetate Dihydrate. *Mater. Chem. Phys.* **2009**, *113*, 334–337.
- (16) Vigneashwari, B.; Dash, S.; Tyagi, A. K.; Parameswaran, P.; Ravichandran, V.; Sunthathiraraj, S. A. Synthesis, Characterization and Assembly of β - In_2S_3 Nanoparticles. *J. Nanosci. Nanotechnol.* **2007**, *7*, 2087–2091.
- (17) Das, K.; De, S. K. Optical Properties of the Type-II Core-Shell TiO_2/CdS Nanorods for Photovoltaic Applications. *J. Phys. Chem. C* **2009**, *113*, 3494–3501.
- (18) Kar, A.; Datta, A.; Patra, A. Fabrication and Optical Properties of Core/Shell $\text{CdS}/\text{LaPO}_4:\text{Eu}$ Nanorods. *J. Mater. Chem.* **2010**, *20*, 916–922.
- (19) Qamar, M.; Kim, S. J.; Ganguli, A. K. TiO_2 -Based Nanotubes Modified with Nickel: Synthesis, Properties, and Improved Photocatalytic Activity. *Nanotechnology* **2009**, *20*, 455703–455711.
- (20) Zhou, M.; Zhang, J.; Cheng, B.; Yu, H. Enhancement of Visible-Light Photocatalytic Activity of Mesoporous Au-TiO_2 Nanocomposites by Surface Plasmon Resonance. *Int. J. Photoenergy* **2012**, *2012*, 532853–532863.
- (21) Wang, Q.; Pan, D.; Jiang, S.; Ji, X.; An, L.; Jiang, B. Luminescent CdSe and CdSe/CdS Core-Shell Nanocrystals Synthesized via a Combination of Solvothermal and Two-Phase Thermal Routes. *J. Lumin.* **2006**, *118*, 91–98.
- (22) Hines, M. A.; Guyot-Sionnest, P. Synthesis and Characterization of Strongly Luminescing ZnS-Capped CdSe Nanocrystals. *J. Phys. Chem.* **1996**, *100*, 468–471.
- (23) Dabbousi, B. O.; Rodriguez-Viejo, J.; Mikulec, F. V.; Heine, J. R.; Mattoussi, H.; Ober, R.; Jensen, K. F.; Bawendi, M. G. CdSe/ZnS Core-Shell Quantum Dots: Synthesis and Characterization of a Size Series of Highly Luminescent Nanocrystallites. *J. Phys. Chem. B* **1997**, *101*, 9463–9475.
- (24) Peng, X. G.; Schlamp, M. C.; Kadavanich, A. V.; Alivisatos, A. P. Epitaxial Growth of Highly Luminescent CdSe/CdS Core/Shell Nanocrystals with Photostability and Electronic Accessibility. *J. Am. Chem. Soc.* **1997**, *119*, 7019–7029.
- (25) Manna, L.; Scher, E. C.; Li, L.-S.; Alivisatos, A. P. Epitaxial Growth and Photochemical Annealing of Graded CdS/ZnS Shells on Colloidal CdSe Nanorod. *J. Am. Chem. Soc.* **2002**, *124*, 7136–7145.
- (26) Ghosh, P.; Kar, A.; Patra, A. Structural and Photoluminescence Properties of Doped and Core-Shell $\text{LaPO}_4:\text{Eu}^{3+}$ Nanocrystals. *J. Appl. Phys.* **2010**, *108*, 113506–113513.
- (27) Chen, W.; Bovin, J.-O.; Joly, A. G.; Wang, S.; Su, F.; Li, G. Full-Color Emission from In_2S_3 and $\text{In}_2\text{S}_3:\text{Eu}^{3+}$ Nanoparticles. *J. Phys. Chem. B* **2004**, *108*, 11927–11934.
- (28) Xu, F.; Vyacheslav, V.; Yimei, Z.; Hanying, B.; Rea, A.; Valappil, N. V.; Su, W.; Gao, X.; Kuskovsky, I. L.; Matsui, H. Long Electron-Hole Separation of ZnO-CdS Core-Shell Quantum Dots. *J. Phys. Chem. C* **2009**, *113*, 19419–19423.
- (29) Kar, A.; Kundu, S.; Patra, A. Photocatalytic Properties of Semiconductor SnO_2/CdS Heterostructure Nanocrystals. *RSC Adv.* **2012**, *2*, 10222–10230.
- (30) Tak, Y.; Hong, S. J.; Lee, J. S.; Yong, K. Fabrication of ZnO/CdS Core/Shell Nanowire Arrays for Efficient Solar Energy Conversion. *J. Mater. Chem.* **2009**, *19*, 5945–5951.
- (31) Zhang, Z.; Wang, W.; Wang, L.; Sun, S. Enhancement of Visible-Light Photocatalysis by Coupling with Narrow-Band-Gap Semiconductor: A Case Study on $\text{Bi}_2\text{S}_3/\text{Bi}_2\text{WO}_6$. *ACS Appl. Mater. Interfaces* **2012**, *4*, 593–597.
- (32) Lahiri, J.; Batzill, M. Surface Functionalization of ZnO Photocatalysts with Monolayer ZnS. *J. Phys. Chem. C* **2008**, *112*, 4304–4307.
- (33) Xiao, Q.; Si, Z.; Zhang, J.; Xiao, C.; Tan, X. Photoinduced Hydroxyl Radical and Photocatalytic Activity of Samarium-Doped TiO_2 Nanocrystalline. *J. Hazard. Mater.* **2008**, *150*, 62–67.
- (34) Kislov, N.; Lahiri, J.; Verma, H.; Goswami, D. Y.; Stefanakos, E.; Batzill, M. Photocatalytic Degradation of Methyl Orange over Single Crystalline ZnO: Orientation Dependence of Photoactivity and Photostability of ZnO. *Langmuir* **2009**, *25*, 3310–3315.
- (35) Yang, Y.; Kim, D. S.; Qin, Y.; Berger, A.; Scholz, R.; Kim, H.; Knez, M.; Gösele, U. Unexpected Long-Term Instability of ZnO Nanowires “Protected” by a TiO_2 Shell. *J. Am. Chem. Soc.* **2009**, *131*, 13920–13921.